33rd Annual International Conference of the IEEE EMBS
Boston, Massachusetts USA, August 30 - September 3, 2011

Towards Segmentation of the Thymus in Fat and Water Parametric MR Images

Sokratis Makrogiannis, Ramona Ramachandran, Kenneth W. Fishbein
Dimitrios Kapogiannis, Richard G. Spencer and Chee W. Chia

Abstract— **The thymus, an organ responsible for the development, selection, and maintenance of the peripheral T-cell population, is an important regulator of the immune system. Despite its physiological significance, it has received little attention in the medical image analysis literature. In practice, the anatomical location and variable shape of this gland pose challenges both in the image acquisition and analysis processes. We present an automated method for segmenting the thymus from water and fat parametric MR images that permits further analysis of volumetrics and tissue characterization. We compute fat ratio and water ratio parametric images and introduce the use of a stochastic edge detector that is embedded in a geometric variational segmentation model. Validation experiments of the proposed algorithm against manual delineations of the thymus indicate the applicability of our approach.**

I. Introduction

The thymus is an organ responsible for the development, selection, and maintenance of the peripheral T-cell population. Age-associated decline in immune function is believed to lead to an increased susceptibility to infection, autoimmunity, and malignancy in older adults. Thymic involution, a process in which thymic parenchyma responsible for T-cell production becomes progressively replaced by adipocytes, which leads to a reduction in naïve T-cell output, may be one of the major contributors to the alteration of the immune system with aging [1], [2]. There has been considerable interest in developing interventional strategies, such as growth hormone administration, to either restore T-cell production in the involuted thymus or slow its rate of decline [3]. Non-invasive methods for quantifying thymic fat and epithelial tissues are needed so that the effects of these interventional strategies on the thymus can be quantified.

A key step towards characterization of thymus size and composition is the delineation of the thymus boundaries from other tissues that can be achieved by image segmentation algorithms. Image segmentation is an important component in many image understanding and computer vision systems with wide applicability in the biomedical imaging field [4], [5], [6], and recent interest that is concentrated on low contrast structures [7], [8], [9]. Nevertheless, the image-based quantification of thymus has been sporadically revisited in the literature [10], [11] and no thymus-specific segmentation algorithm has been proposed so far to the best of our knowledge. Due to its anatomical location just superior and anterior to the heart, the thymus is subject to respiratory and cardiac motion, so MR imaging of the thymus becomes a non-trivial task. An example of parametric water and fat thymus images is displayed in Figure 1. In addition, the shape and size of thymus are highly variable between individuals - as seen in Figure 2- making the segmentation task even more complicated.

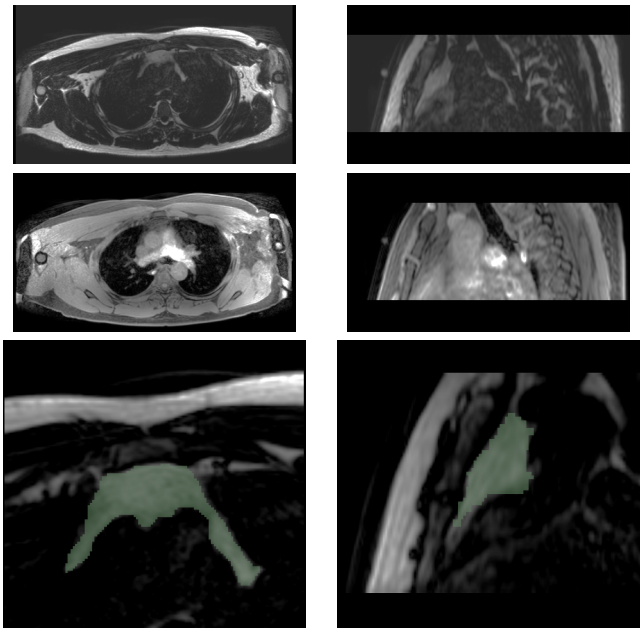

Fig. 1: Images depicting the location of the thymus in axial (left) and sagittal (right) views. First and second rows: fat and water Dixon MRI of the same participant. Third row: manually segmented thymus region marked with green color. Because of cardiac and respiratory motion, the boundaries between the thymus and adjacent tissues frequently appear blurred and/or discontinuous.

Here we introduce a segmentation method that is based on geometric model segmentation that uses a stochastic approach for identification of the image edges. After acquisition of parametric water and fat MR images with the 3-point Dixon method [12], we compute fat-ratio parametric images to be used as input to the segmentation algorithm. We extend a Parzen-based stochastic edge estimator to the volumetric

All authors are affiliated with the National Institute on Aging, National Institutes of Health, 3001 S. Hanover St., Baltimore, MD 21225, USA. Corresponding author email: makrogianniss@mail.nih.gov

This research was supported entirely by the Intramural Research Program of the NIH, National Institute on Aging.

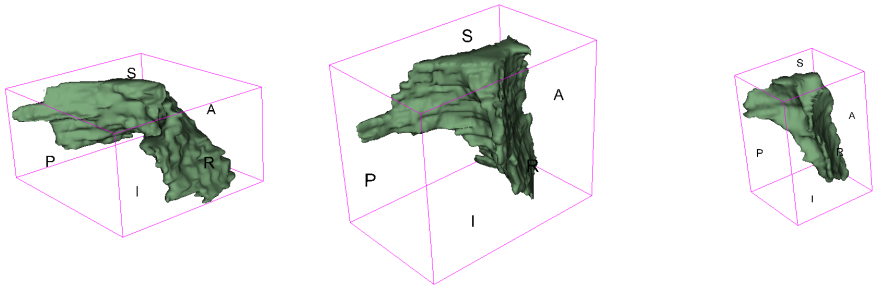

Fig. 2: Three manual segmentations of the thymus of different participants in our dataset. We note here the highly variable thymus anatomy; the volumes of the displayed thymus masks are 43.97 mL (left), 66.4 mL (middle) and 12.6 mL (right) respectively.

image domain and embed it in the level-set segmentation framework. In the experimental section we extensively test our method against reference masks produced by manual segmentation and examine the effects of the use of parametric images and stochastic edge detector for segmentation versus more conventional approaches.

II. Background: Geodesic active contours

Our goal is to delineate the thymus by addressing difficulties caused by discontinuous boundaries, low contrast and highly variable anatomical shape and size. Our preliminary tests showed that simple region growing or centroid clustering techniques typically over-detect the thymus. On the contrary, parametric and geometric deformable models have produced encouraging segmentation results when applied to biomedical imaging data. A sub-group of geometric deformable models is implemented by the level-set formulation, which embeds the propagating surface in a higher dimensional function that evolves with time in the Eulerian coordinate system under a wavefront propagation PDE.

In this work we use the geodesic active contours algorithm by Casselles et al [13] that uses a geodesic minimization framework to define a geometric flow PDE:

$$\frac{\partial u}{\partial t} = g\left(I\right)\left(c+\kappa\right)|\nabla u| + \nabla u \cdot \nabla g\left(I\right), \qquad (1)$$

where u is the level set function, g is the edge stopping function computed from the image and c is a constant velocity factor to facilitate faster convergence to the object boundary. The function g is positive and strictly decreasing, typically computed from the gradient magnitude of the image I as $g = \frac{1}{1+|\nabla \hat{I}|^q}$, where $\hat{I}$ is a smoothed version of I and q = 1 or 2. The use of a simple gradient magnitude operator works well for well defined boundaries but is susceptible to error in the presence of discontinuous or blurred boundaries or noisy region interiors.

Here we propose a more robust solution by computing the edge probability using non-parametric probability density estimation in the local neighbourhood of each voxel. We also propose to detect the edges in the feature domain defined by the signal intensity of the fat-ratio images.

III. Computation of Fat-ratio Images

In MRI techniques the signal intensity range may differ significantly between different imaging sessions. This discrepancy complicates the automation of further analysis of these datasets. In order to overcome this difficulty we compute the fat-ratio (FR) image from the acquired fat (F) and water (W) images using voxel-wise algebraic operations:

$$FR(\mathbf{w}) = F(\mathbf{w}) / \left[F(\mathbf{w}) + W(\mathbf{w})\right] \qquad (2)$$

where $\mathbf{w}$ denotes the spatial coordinates in the d-dimensional space, $\mathbf{w} \in N^d$. The FR voxel intensities range in the more amenable space of $[0, 1]$. Still, the main pitfall of using (2) is that it produces very high intensities in regions filled with air because the denominator becomes very small. The correct signal intensity of these regions should be zero since they contain neither fat nor water; the signal in these regions is noise despite its high intensity. We address this issue by computing the summation of F and W and then applying Otsu multiple thresholding –with number of classes $C = 4$– to the resulting sum. We label the group of the smallest intensity as air and set the voxels belonging to this group to zero in the previously computed FR. This results in suppression of the voxel intensities corresponding to air. It is worth noting that we can also compute a water ratio image WR following similar steps as above. An example of the intermediate and final stages of fat ratio computation with air voxel suppression is illustrated in Figure 3.

IV. Stochastic Edge Estimation

We extend the formulation of the stochastic edge estimator proposed in [14] to volumetric medical imaging data and use it in the level-set framework to drive thymus segmentation. The rationale behind this edge estimator assumes that the image intensity field can be locally approximated by homogeneous regions or edges. The probability density function in the first case can be approximated by a unimodal distribution and in the second case by a bimodal distribution. An index of bimodality is given by the probability density of the samples' mean. As explained in [14] in the case of a homogeneous

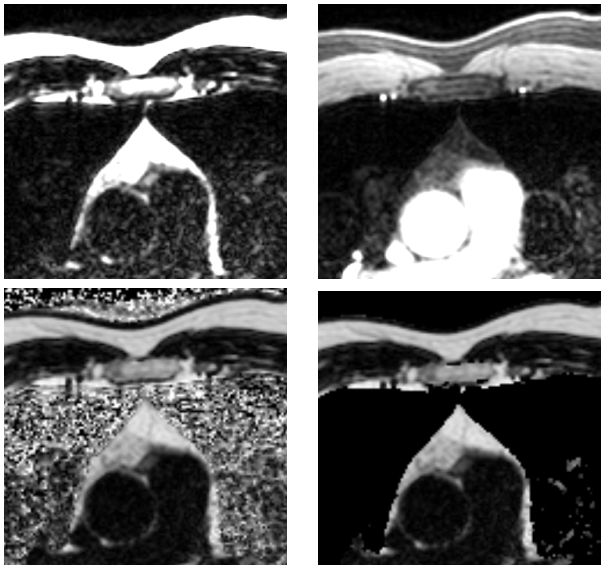

Fig. 3: Example of computation of a fat ratio image and removal of regions filled with air. Top row: fat (left) and water (right) Dixon images of the thymus in the same participant. Bottom row: fat-ratio parametric image before (left), and after (right) removal of the air regions. The voxels corresponding to air take on high values because of low signal intensities in both the fat and water images.

region the likelihood of the mean will be high, whereas for an edge the likelihood of the mean will be low.

We estimate the probability density by a non-parametric technique in order to avoid errors caused by the small sample size and the presence of noise. In addition, non-parametric techniques have the advantage that they do not make any explicit assumptions about the underlying distribution; rather, the data samples are used as models. Here we use the widely known non-parametric technique of Parzen kernels. The probability density estimate $\tilde{f}(\mathbf{X})$ of a function f at point $\mathbf{X}$ is computed by:

$$\tilde{f}\left(\mathbf{X}\right) = \frac{1}{Nh^p} \sum_{i=1}^{N} K\left(\frac{\mathbf{X} - \mathbf{X}_i}{h}\right) \tag{3}$$

In this equation K is the kernel function, which is usually of Gaussian type, h is the Parzen bandwidth parameter, which controls the desired level of detail in edge estimation, $\mathbf{X}_i$ is the sample at index i in the kernel window W, N is the number of samples inside the kernel and p is the dimensionality of variable $\mathbf{X}$. The edge map is computed by sliding the window W, estimating the probability density at the mean vector of the voxel intensities inside W and assigning the probability density to the center voxel. In this way we form an d-dimensional image with the same attributes as the input.

V. Experiments and Discussion

We acquired the images using a Philips 3T Achieva scanner equipped with a 32-channel cardiac/torso coil, pneumatic respiration sensor and MRI-compatible vector cardiogram (VCG) unit. We first performed a single-echo 3D fast field echo (eTHRIVE) scan within one 20 second breath-hold, and then divided the thymus extent along the superior-inferior axis into 4 to 8 contiguous groups of 10 axial slices. We scanned each group in a single 20 second breath-hold using a 3-point Dixon [12] eTHRIVE sequence with 1.5 mm isotropic voxels, field of view $360 \times 400 \times 150mm$ $(A/P \times R/L \times H/F)$, SENSE acceleration factor $1.8 \times 1 (R/L \times H/F)$, $flip\ angle$=10 °, $NEX = 1$, $TR = 3ms$ and $TE = 1.4ms$. To ensure reproducible breath-holds we displayed and recorded the respiratory sensor absolute pressure on a PowerLab data acquisition system (AD Instruments).

We applied the segmentation algorithm to 15 datasets and validated it against reference thymus masks provided by RR and SM. The test data were divided into two groups and each reader manually delineated the thymi of one group using the MIPAV software package (NIH, Bethesda, MD). We then executed our automated algorithm over the same database and computed measures of overlap, classification accuracy and the Dice score [15] between the reference and tested methods. An example of manual and automated segmentation on one of our datasets is displayed in Figure 4.

We re-tuned the key parameters of the Parzen edge estimator and the geodesic active contours following exhaustive search optimization of the DICE score. We first defined the parameters, range (lower and upper bounds) and granularity (the number of samples) of the search space. We then executed the segmentation algorithm over the complete database and computed validation score statistics for each parameter setting in the search space. We ranked the average Dice scores and selected the algorithm parameters producing the best performance.

In the validation experiments, we concentrated on the effectiveness of the key elements in our approach. In the first experiment we compared the segmentation accuracy produced by different input images to our algorithm, i.e., the fat-ratio only FR, joint Dixon fat and water images $\{F, W\}$ and the Dixon fat image F only. In Table I, we observe that FR images produce clearly more accurate thymus segmentation than the paired analysis of Dixon fat and water images $\{F, W\}$ or the analysis of Dixon fat images F only. The main reason for this is that the FR image intensities are restricted in [0,1] therefore are more amenable to segmentation, whereas the original voxel intensities of F and W images may vary between different image acquisitions. Further, the suppression of noise in the air regions of the FR images significantly facilitates the edge estimation and level-set segmentation processes. We also note that the joint analysis of the F and W images outperforms the F only analysis because the additional component W improves the separation between the thymus and its adjacent tissues.

An additional experiment was to compare the segmentation produced by the reported probabilistic edge map with the conventional gradient magnitude. The experimental results presented in Table I show a small improvement in Dice score when the stochastic edge map is used. A qualitative

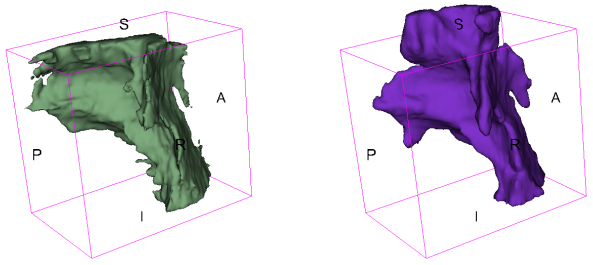

Fig. 4: Manually segmented reference mask (left) and automated segmentation result (right) in the physical space.

TABLE I: Average Dice scores and averages of Dice score differences produced by our segmentation algorithm after using the stochastic (S) or gradient magnitude-based edge detector (G), applied to the fat ratio image only (FR), or the joint Dixon fat and water images ($\{F, W\}$), or the Dixon fat images only (F).

Algorithm	**Ave. Dice S.**	**Algorithm**	**Ave. Dice S.**
S_{FR}	0.691	G_{FR}	0.686
$S_{\{F,W\}}$	0.5	$G_{\{F,W\}}$	0.488
S_F	0.362	G_F	0.396
Comparison	**Ave. Diff.**	**Comparison**	**Ave. Diff.**
$S_{FR} - G_{FR}$	0.005	$S_{FR} - S_{\{F,W\}}$	0.19
$S_{\{F,W\}} - G_{\{F,W\}}$	0.013	$S_{\{F,W\}} - S_F$	0.138

comparison suggests that the stochastic edge map always produces a standardized probability map that can be easily manipulated in subsequent analysis whereas the gradient magnitude range will vary depending on the range of the input values. In addition, the sensitivity of Parzen-based edge estimation can be adjusted by the Parzen kernel bandwidth h that is expected to be advantageous in a multiple scale analysis scheme, whereas the gradient magnitude operators could be modified only by application of pre-filtering to the original image. On the other hand, the gradient-based edge detection is computationally simpler, saving execution time.

In conclusion, we have presented a systematic method for segmentation of the thymus using fat and water parametric MR imaging data. To the best of our knowledge, this is the first report of automated segmentation of the thymus in MR images. A key element of this work is the computation of parametric fat-ratio and water-ratio images from the fat and water images that were originally acquired. The fat-ratio and water-ratio parametric images were found to be more amenable to segmentation mainly due to the restricted range of voxel intensities. Another significant advantage of these images is that they can be readily used for characterization of thymus composition, which is one of the clinical applications of this method. We should also note the first use of a Parzen-based edge estimator in a variational framework. This method produces scaled output in [0,1] and can be applied at variable levels of detail controlled by the Parzen bandwidth. Another desirable property is that this stochastic edge estimator can be readily extended to d-dimensional domains for vectorial image analysis. The validation against manual thymus delineations indicates that the proposed approach produces encouraging results and can address challenges posed by the thymus' anatomical location, as well as its variability in shape and size. Future work will be directed towards addition of more test data, evaluation of manual segmentation variability, and improvement of segmentation accuracy.

REFERENCES

[1] D. D. Taub and D. L. Longo, "Insights into thymic aging and regeneration." *Immunol Rev*, vol. 205, pp. 72–93, Jun 2005. [Online]. Available: http://dx.doi.org/10.1111/j.0105-2896.2005.00275.x

[2] B. F. Haynes, G. D. Sempowski, A. F. Wells, and L. P. Hale, "The human thymus during aging." *Immunol Res*, vol. 22, no. 2-3, pp. 253–261, 2000. [Online]. Available: http://dx.doi.org/10.1385/IR:22:2-3:253

[3] D. D. Taub, W. J. Murphy, and D. L. Longo, "Rejuvenation of the aging thymus: growth hormone-mediated and ghrelin-mediated signaling pathways." *Curr Opin Pharmacol*, vol. 10, no. 4, pp. 408–424, Aug 2010. [Online]. Available: http://dx.doi.org/10.1016/j.coph.2010.04.015

[4] A. K. Jain, M. N. Murty, and P. J. Flynn, "Data clustering: a review," *ACM Comput. Surv.*, vol. 31, no. 3, pp. 264–323, Sep 1999.

[5] C. Xu and J. L. Prince, "Snakes, shapes, and gradient vector flow," *IEEE Transactions on Image Processing*, vol. 7, no. 3, pp. 359–369, 1998. [Online]. Available: http://dx.doi.org/10.1109/83.661186

[6] R. Malladi, J. A. Sethian, and B. C. Vemuri, "Shape modeling with front propagation: A level set approach," *IEEE Transactions on Pattern Analysis and Machine Intelligence*, vol. 17, pp. 158–175, 1995.

[7] Y. Rathi, O. Michailovich, J. Malcolm, and A. Tannenbaum, "Seeing the unseen: Segmenting with distributions," in *International Conference on Signal and Image Processing*, 2006.

[8] S. Makrogiannis, R. Bhotika, J. V. Miller, J. Skinner, and M. Vass, "Nonparametric intensity priors for level set segmentation of low contrast structures," in *MICCAI (1)*, 2009, pp. 239–246.

[9] M. Depa, M. R. Sabuncu, G. Holmvang, R. Nezafat, E. J. Schmidt, and P. Golland, "Robust atlas-based segmentation of highly variable anatomy: left atrium segmentation," in *Proceedings of the First international conference on Statistical atlases and computational models of the heart, and international conference on Cardiac electrophysiological simulation challenge*, ser. STACOM'10/CESC'10. Berlin, Heidelberg: Springer-Verlag, 2010, pp. 85–94. [Online]. Available: http://portal.acm.org/citation.cfm?id=1889198.1889210

[10] K. Takahashi, T. Inaoka, N. Murakami, H. Hirota, K. Iwata, K. Nagasawa, T. Yamada, M. Mineta, and T. Aburano, "Characterization of the normal and hyperplastic thymus on chemical-shift mr imaging." *AJR Am J Roentgenol*, vol. 180, no. 5, pp. 1265–1269, May 2003.

[11] G. M. Fahy, "Apparent induction of partial thymic regeneration in a normal human subject: A case report," *Journal of Anti-Aging Medicine*, vol. 6, no. 3, pp. 219–227, 2003.

[12] G. H. Glover and E. Schneider, "Three-point dixon technique for true water/fat decomposition with b0 inhomogeneity correction." *Magn Reson Med*, vol. 18, no. 2, pp. 371–383, Apr 1991.

[13] V. Caselles, R. Kimmel, and G. Sapiro, "Geodesic active contours," *International Journal of Computer Vision*, vol. 22, no. 1, pp. 61–79, 1997. [Online]. Available: http://dx.doi.org/10.1023/A:1007979827043

[14] G. Economou, A. Fotinos, S. Makrogiannis, and S. Fotopoulos, "Color image edge detection based on nonparametric density estimation," in *Proc. International Conference on Image Processing*, vol. 1, Oct. 7–10, 2001, pp. 922–925.

[15] L. R. Dice, "Measures of the Amount of Ecologic Association Between Species," *Ecology*, vol. 26, no. 3, pp. 297–302, July 1945.